ADVANCED FUNCTIONAL MATERIALS
www.afm-journal.de

Impact of Blend Morphology on Interface State Recombination in Bulk Heterojunction Organic Solar Cells

Benjamin Bouthinon, Raphaël Clerc, Jérôme Vaillant, Jean-Marie Verilhac, Jérôme Faure-Vincent, David Djurado, Irina Ionica, Gabriel Man, Antoine Gras, Georges Pananakakis, Romain Gwoziecki, and Antoine Kahn*

This work is a reinvestigation of the impact of blend morphology and thermal annealing on the electrical performance of regioregular-P3HT:$PC_{60}BM$ bulk heterojunction organic solar cells. The morphological, structural, and electrical properties of the blend are experimentally investigated with atomic force microscopy, X-ray diffraction, and time-of-flight measurements. Current–voltage characteristics of photodiode devices are measured in the dark and under illumination. Finally, the existence of exponential electronic band tails due to gap states is experimentally confirmed by measuring the device spectral response in the subband gap regime. This method reveals the existence of a large density of gap states, which is partially and systematically reduced by thermal annealing. When the band tails are properly accounted for in the drift and diffusion simulations, experimentally measured charge transport characteristics, under both dark and illuminated conditions and as a function of annealing time, can be satisfactorily reproduced. This work further confirms the critical impact of tails states on the performance of solar cells.

1. Introduction

Large device area, low weight, cost effectiveness, and mechanical flexibility are some of the exciting properties of printed organic solar cells.[1–4] Since the introduction of the organic diode concept by Tang *et al*. in 1986,[5] the performance of printed organic devices has improved considerably, reaching a record power conversion efficiency (PCE) of 11.1%.[6]

The Bulk HeteroJunction solar cell (BHJ) is one of the most common types of printed organic photovoltaic devices.[7] This structure offers not only an excellent trade-off between optimal charge transfer[8] and exciton dissociation at the donor/acceptor interface,[9] but also good collection of photogenerated carriers.

As many investigators have pointed out[10–13] the intimate organization of the interpenetrating network composed of the acceptorlike material (fullerene) and the donorlike material (polymer) is of critical importance, since it directly impacts the electro-optical performance of the cell. Indeed, photon absorption, exciton dissociation, and carrier collection are all morphology-dependent parameters.[9,14–17]

For this reason, the optimization of BHJ blend morphology has been extensively investigated, essentially via atomic force microscopy (AFM) phase imaging[18] or transmission electron microscopy (TEM).[19,20] Changes in blend crystallization are typically probed using X-ray diffraction (XRD).[21] In these aforementioned investigations, parameters impacting the morphology were identified, such as the nature of the solvent,[22] the use of solvent additives,[23,24] the deposition method,[25,26] the polymer/fullerene ratio,[27,28] the polymer and fullerene crystallization state,[12,29–32] the nature of the fullerene material,[33] and the effects of blend annealing (duration, temperature), which is one of the most heavily studied parameters.[34,35]

The understanding of the relationship between cell efficiency and morphology has recently advanced. Several authors have simulated the performance of BHJ organic solar cells, explicitly accounting for blend morphology and using kinetic Monte Carlo[11,17,36,37] or 3D drift and diffusion approaches.[38,39] These studies concluded that an optimal morphology exists, and it is determined by the trade-off between exciton dissociation (penalized by overly large blend domains) and Langevin recombination (enhanced by overly narrow blend domains).

This picture is still incomplete, however, as it ignores another significant recombination mechanism: trap-assisted recombination. Street and co-workers[40,41] have shown trap-assisted

Dr. B. Bouthinon, Dr. J. Vaillant, Dr. J.-M. Verilhac, A. Gras, Dr. R. Gwoziecki
CEA, LITEN, Laboratoire des Composants Electroniques Imprimés
F-38054, Grenoble, France
E-mail: bouthinon.benjamin@gmail.com
Prof. R. Clerc
Laboratoire Hubert Curien, UMR CNRS 5516
Université Jean Monnet
Institut d'Optique Graduate School
F-42000, Saint-Etienne, France
Dr. J. Faure-Vincent, Dr. D. Djurado
CEA, INAC, Structure des Propriétés d'Architectures Moléculaires
UMR5819
F-38054, Grenoble, France
Dr. I. Ionica, Prof. G. Pananakakis
IMEP LAHC, Grenoble INP – Minatec
F-38016, Grenoble, France
G. Man, Prof. A. Kahn
Department of Electrical Engineering
Princeton University
Princeton, NJ 08544, USA

DOI: 10.1002/adfm.201401633

recombination to be one of the major sources of PCE losses in poly(3-hexylthiophene-2,5-diyl) (P3HT):[6,6]-phenyl-C61-butyric acid methyl ester ($PC_{60}BM$) and poly[N-9′-heptadecanyl-2,7-carbazole-alt-5,5-(4′,7′-di-2-thienyl-2′,1′,3′-benzothiadiazole)] (PCDTBT):[6,6]-phenyl-C71-butyric acid methyl ester ($PC_{70}BM$) solar cells.[42,43] This conclusion was reached using spectral response measurements in the near IR region, probing sub-band gap transitions from trap levels to the HOMO or LUMO levels. However, as the measurements were performed on devices with a given morphology, little was extracted about the correlation between morphology and trap distribution and density.

It is well known that either Langevin or trap-assisted recombination occurs mostly at the donor–acceptor interface. For this reason, it is unclear whether annealing impacts device performance mostly by changing the morphology of the blend (i.e., interface volume fraction) or by modifying the recombination properties of the blend (transport properties, trap concentration).

The aim of this study is to investigate the impact of morphology on trap-assisted recombination in BHJ solar cells. In this contribution, the blend morphology is systematically modified by means of successive post-deposition thermal treatments at 85 °C. Both the blend morphology and key solar cell properties are characterized for each annealing treatment. The spectral response of the device in the near infrared (NIR) region is measured to probe how the gap states evolve with annealing duration. In addition, a numerical model (based on a one-dimensional drift–diffusion formalism), properly calibrated with experiments, is implemented, accounting for the measured exponential density of trap states. The conclusions obtained from comparing experiments and simulations are discussed in the last section of the paper.

2. Sample Preparation

Devices used in this study had the following general structure: ITO/PEDOT:PSS/P3HT:$PC_{60}BM$/Al. Regioregular poly(3-hexylthiophene-2,5-diyl) (P3HT) and phenyl-C_{61}-butyric acid methyl ester ($PC_{60}BM$) were purchased from Merck. Poly(3,4-ethylenedioxythiophene) (PEDOT:PSS), branded as CLEVIOS P VP AI 4083, was purchased from Heraeus.

ITO-coated glass substrates were cleaned by ultrasonicating them in EDI (electrodeionized water), acetone, and isopropanol for 10 min each. The hole-injecting PEDOT:PSS layer was spin-coated at 2000 RPM for 50 s to form a 40 nm film on top of the ITO substrate. The samples were subsequently dehydrated at 115 °C in nitrogen for 20 min. A 50 mg mL^{-1} solution of P3HT:$PC_{60}BM$ was solubilized in chlorobenzene with a blend ratio of 1:1 (weight ratio). Diiodooctane (DIO) was added to the solution (5% in volume) to selectively dissolve the fullerene molecules and avert C_{60} aggregation.[24,44,45] While the chlorobenzene is evaporating after the blend layer has been spin-coated, the DIO additive maintains the solubility of the fullerene in the semicrystalline P3HT matrix, as its melting point is higher than that of chlorobenzene (169 vs 131 °C). DIO has been used in all experiments, specifically to improve the degree of crystallinity of P3HT domains (see later). The P3HT:$PC_{60}BM$ blend layer was spin-coated at 800 RPM for 3 min in air. The typical thickness of the active layer was 330 nm, as measured by a mechanical profilometer. The large thickness of the active layer, which is detrimental to solar cell performance, is needed in this work, in order to keep the level of dark current low. Indeed, it would no longer be possible to accurately measure the external quantum efficiency (EQE) at low photon energy if the dark current is too large. No annealing treatment was performed after the blend layer had been deposited. Finally, 100 nm thick aluminum electrical contacts (serving as cathodes) were vacuum-evaporated using a shadow mask, in a vacuum chamber at a pressure of 10^{-6} mbar. Completed devices were stored for one day in a nitrogen-filled glove box and then encapsulated with a glass cover. The device area was 3.14 mm^2.

For the thermal annealing treatments, the encapsulated solar cell was annealed on a hot plate at 85 °C in nitrogen. The temperature was selected to mitigate diffusion of the C_{60}, which is usually observed at higher annealing temperatures.[13]

3. Experimental Results

3.1. Physical Characterization of the Blend Morphology

AFM tapping mode measurements were performed on the surfaces of P3HT:$PC_{60}BM$ blend films, which were subjected to different annealing treatments, in order to monitor how the average domain width evolves with annealing. Topography and phase were both recorded during the scans and the results are shown in Figure S1, Supporting Information. Phase measurements are known to reveal crystallized regions,[18,46] the identification of which is aided by the fibrous nature of P3HT. The average width of the P3HT domains is extracted from AFM phase images, using an autocorrelation procedure performed numerically on the raw data. In accordance with the findings of Dante et al.,[18] we measured an increase in the average domain width with annealing (**Figure 1**). Moreover, this domain growth

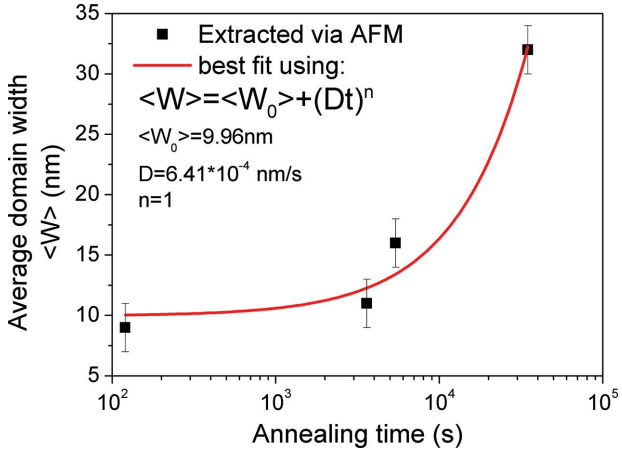

Figure 1. Average domain width extracted from AFM images versus annealing time. Symbols refer to experiments; line to a fitting obtained using the theoretical law proposed in the work of Ray and Alam.[47]

is found to follow the kinetics introduced by Ray and Alam,[47] given by

$$\langle W(t)\rangle = \langle W_0\rangle + (D_{\text{eff}}t)^n \quad (1)$$

where $\langle W_0\rangle$ is the initial average domain width, D_{eff} is the effective diffusivity of the organic/polymer material, and n is the "Lifshitz–Slyozov" power exponent associated with spinodal decomposition. The following parameters were found after fitting the experimental data:

$$\langle W_0\rangle = 9.96\ \text{nm} \cdot D_{\text{eff}} = 6.41 \times 10^{-4}\ \text{nm s}^{-1} \cdot n = 1$$

This result not only confirms the validity of Equation (1), but also demonstrates how this simple approach can be used to estimate the increase in average domain width during the thermal annealing experiments.

X-ray diffraction (XRD) experiments, conducted using the Bragg Brentano ($\theta/2\theta$) reflection diffraction geometry and a cobalt radiation source (λ = 1.789 Å), were performed on P3HT:$PC_{60}BM$ films deposited onto ITO-coated glass, in order to estimate the average growth of P3HT crystallites in the transverse direction (perpendicular to the substrate). The raw data was corrected by subtracting the background signal originating from the ITO-coated glass substrate reference. The intense (h00) reflections along the q_z direction indicate the formation of a lamellar structure with the side chains oriented out of the plane of the substrate, as illustrated in **Figure 2**a. This result is typical of films formed from semicrystalline π-conjugated polymers such as P3HT. The (0k0) reflections corresponding to the π–π interchain stacking period were not visible in the spectra, confirming its in-plane orientation[48] (see Figure S2, Supporting Information, for complete XRD spectra). The coherence length (crystallite size) is measured from the (100) reflection peak using the Scherrer formula and a fitted Pseudo-Voigt peak shape function. The interchain distance **a** is found to be 16.5 Å from the peak analysis, a value consistent with reported literature values for P3HT.[31] In Figure 2b, the coherence length of the P3HT extracted from the (100) peak is reported as function of the annealing time.

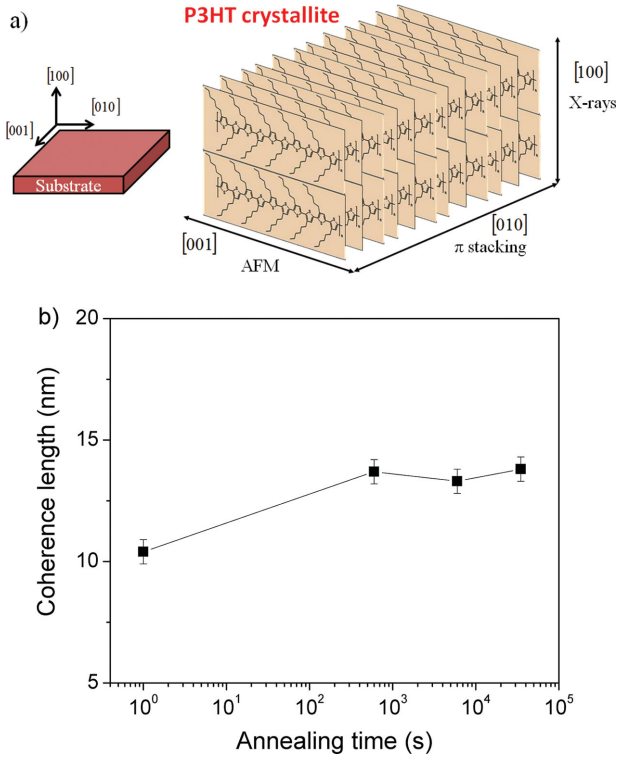

Figure 2. a) Schematic representation of the orientation of ordered P3HT domains with side chains perpendicular to the substrate; b) Coherence length extracted from X-rays diffraction spectra at the identified (001) peak using the Scherrer formula.

We conclude from the AFM and XRD measurements that the internal structure of P3HT fibrils as seen by AFM consists in a self-organization of P3HT chains in a lamellalike structure whose stacking period is given by the position of the (100) Bragg peak. The in-plane organization has also been confirmed by AFM phase measurements. Moreover, the coherence length L_c corresponding to the average size of P3HT crystallites in the transverse direction (perpendicular to the substrate) was also extracted. Only a weak increase was determined during the post-annealing treatment, moving from 10.4 to 13.8 nm, and indicating that the crystallite growth is anisotropic in character since it differs noticeably from the observation made for in-plane morphology as observed by AFM. In summary, P3HT lamellae evolves into a larger scale organization in the (001) direction when introducing annealing.

The P3HT crystallite size evolution versus annealing can thus be deduced from the combination of both AFM and X-rays measurements. With an average crystallite volume approximately given by $L_C\pi\frac{\langle W(t)\rangle^2}{4}$, and given that L_c appears almost constant under annealing, the results indicate that the crystallites volume increases by a factor of 9 during the full duration of the process and its perimeter by a factor of 3.

It has to be noticed that the existence of a third phase in P3HT:$PC_{60}BM$ blend, composed of amorphous finely intermixed regions, has been recently reported.[49–54] AFM and X-rays diffraction techniques are not suitable for the characterization of this third phase. Indeed, in our work, the characterization of the blend morphology has been limited to the monitoring of pure P3HT domains. In principle, additional morphology characterization (such as 2D X-ray scattering in grazing incidence geometry (GIWAXS) as performed in ref. [52] would be needed to further quantify the importance of this third phase. However, the appearance of vibronic bands on the P3HT:PCBM absorption spectra at 550 and 600 nm (see Figure S3, Supporting Information) is a first order indication of a large presence of pure P3HT crystalline phase, as expected when an additive has been used, as suggested in the work of Vongsaysy et al.[55]

3.2. Time of Flight Mobility Measurements

Performance improvements due to annealing have sometimes been attributed to carrier mobility improvements.[21] To address this assumption in the context of the present work, carrier mobility was measured using the TOF technique,[56] which is well suited for mobility measurements in disordered organic

systems such as π-conjugated polymers.[57] The technique, however, cannot be directly applied on the solar cell samples used in this study, as it requires layer thicknesses at least ten times larger than the optical absorption length (approximately 90 nm for P3HT:$PC_{60}BM$ at 530 nm, taking an extinction coefficient of 0.45[58]. Samples used in our TOF experiments were approximately 1 µm thick, i.e., three times thicker than the solar cell active layer used in this work. Except for the active layer thickness, the TOF samples fabrication procedure is identical as described in process details section.

TOF measurements were performed using a 532 nm, 35 µJ cm^{-2}, 1 ns laser beam. The laser intensity was attenuated by insertion of neutral density filters. A chopper was used to select a laser pulse every second. The measured signal was averaged over 50 acquisitions. Both electron and hole mobilities were extracted from TOF signals.

The resulting electron and hole mobilities are plotted for several annealing times and square root of applied electric field in **Figure 3**a,b. Interestingly, the mobility is not significantly modified by annealing. These results appear consistent with the previously mentioned X-ray experiments, which showed basically no evolution with temperature of the crystallite size in the transverse direction (i.e., the photo-generated transport direction in this case).

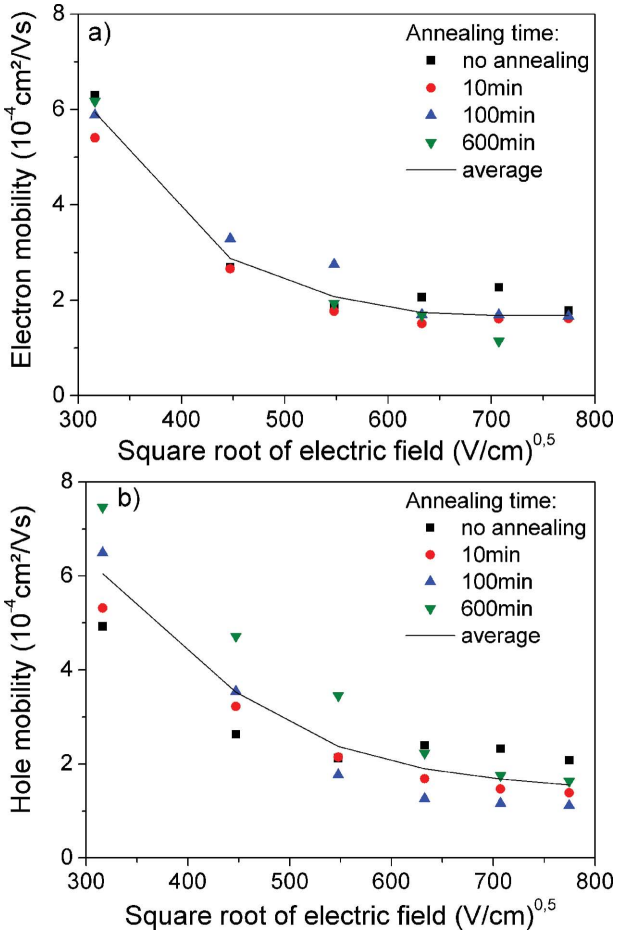

Figure 3. Electron a) and hole b) mobility extracted from time-of-flight measurements, for different annealing times, plotted against the square-root of the electric field. The hole mobility is extracted by illuminating the device from the aluminum cathode electrode, whereas for the electron mobility, the device is illuminated from the glass substrate side.

Similar results were obtained by Mandoc et al.[59] On the other hand, Mihailetchi et al.[21,60] reported a hole-mobility improvement of 4 orders of magnitude for similar measurements. This discrepancy is presumably due to differences in sample preparation (solvent, additive, solid contents). In our work, absorption spectroscopy (see Figure S3, Supporting Information) and X-rays diffraction measurements reveal that the ratio of the volume of crystallized P3HT to the total volume is approximately equal to 60% before annealing. Although this ratio was not specified in the work of Mihailetchi et al., the extreme low value of their hole mobility before annealing ($\approx 10^{-8}$ cm^2 V^{-1} s^{-1}, compared to $\approx 10^{-4}$ cm^2 V^{-1} s^{-1} in our work) suggests a much lower concentration of crystallized P3HT fraction before annealing. Moreover, mobility in that work was not measured by TOF, but extracted from an *I–V* curve fitting using a space charge limited current (SCLC) model, which renders a quantitative comparison with mobility values reported in our work questionable.

Finally, experiments show a decreasing mobility with electric field for both electrons and holes, which is rather unexpected for most polymers, but typical of energetic and spatial disorder in P3HT material.[61,62] Experiments can be fitted by the model proposed in ref. [63]: this empirical model is then used to calibrate numerical simulations.

3.3. Impact of Morphology on *I–V* and Visible EQE Measurements

Photocurrent, EQE, and dark current were measured after each annealing step in order to monitor the impact of annealing on diode performance.

First, photocurrent measurements in the short-circuit condition were performed at two different wavelengths, 440 and 620 nm, corresponding to the absorption peak of $PC_{60}BM$ and P3HT, respectively. Since each wavelength probes a different molecule, the experiment helps to quantify the domain evolution of the polymer and fullerene separately. As previously mentioned, the annealing temperature is limited to 85 °C in order to prevent the vertical phase segregation of $PC_{60}BM$, which is known to appear when the temperature exceeds a certain value.[13] The appearance of this segregation can be detected by monitoring the external quantum efficiency measuring the relative amplitude of $PC_{60}BM$ and P3HT peaks.

The external quantum efficiency as a function of the annealing time is reported on **Figure 4**a. Both curves at 440 nm (fullerene absorption) and 620 nm (polymer absorption) exhibit a similar "bell-shaped" curve. A closer look at Figure 4a. reveals that the two curves follow a similar trend in the left portion of the curve (low domain size regime), but differ right of the maximum. Similar wavelength dependency of the EQE versus annealing time has been previously reported in the literature.[64] The result suggests that the annealing induces a similar change in both polymer and fullerene domains, at least for short annealing time. An alternative explanation, consistent with the conclusions of the next section, is that the mechanisms

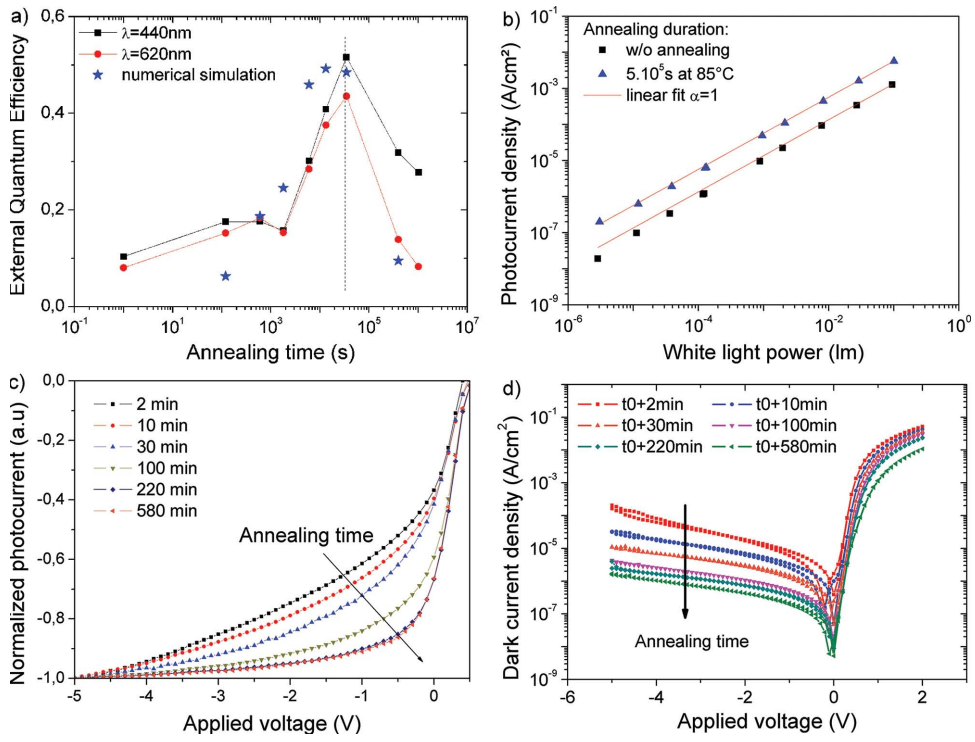

Figure 4. a) Photodiode external quantum efficiency measured in short circuit condition versus the 85 °C annealing duration. The device quantum efficiency is measured at two different wavelengths, corresponding to the maximum absorption of the polymer and the fullerene respectively (620 nm and 440 nm). b) Measured photocurrent density in short circuit condition versus white light power (halogen quartz lamp) for two different annealing durations. Different optical densities are used to modulate the light power. A linear function (line) has been also plotted to visually confirm the linearity of the curves over more than 5 decades. c) Experimental normalized photocurrent versus applied voltage for different annealing durations. The photocurrent normalization consists in dividing by the illuminated current density value at −5 V. The illumination is performed by white light from halogen quartz lamp. d) Measured dark current–voltage characteristics, after different 85 °C annealing duration. Contrary to the photocurrent, the dark reverse current keeps on decreasing with successive annealing steps.

impacting the EQE are not the same in the first and the second part of the curve, and thus are not impacted in the same way by the size of fullerene and polymer domains.

During the first 580 min, the EQE at 440 nm (620 nm) is improved from 15% (8%) up to 37% (47%). After this optimal annealing time, the EQE drops off when additional annealing steps are performed. This drop is usually attributed to the degradation of the exciton dissociation rate, when the domain size exceeds the exciton diffusion length.[65]

The first regime is less well understood, in part because it is somehow difficult to obtain such small values of domain size, especially without introducing additives such as DIO to get an improved interpenetrating network. Some authors attribute this first regime to an excess of Langevin recombination, occurring in blends with large interfacial volume ratio.[11] Others authors attribute this effect to the increase of percolation path connecting both electrodes, making more favorable the carriers collection.[33] As mentioned previously, the photocurrent improvement is sometime also attributed to an enhancement of transport properties induced by polymer crystallization.[30] However, this later assumption appears in contradiction with the TOF mobility measurements reported above. In addition, the absorption spectra indicate an excellent thermal stability, suggesting that the crystallization of the blend occurs mostly during the deposition step and not during the post-thermal treatment (see Figure S3, Supporting Information). The use of additive such as DIO is most likely the cause of such stability. Our interpretation will be discussed in the next section.

Photocurrent was measured as function of incident light flux in order to determine the main recombination mechanism operating in the solar cell. Indeed, the dominant mechanism, Langevin-type recombination versus trap assisted recombination, can be distinguished by monitoring the slope of the photocurrent function of the incident light power. Langevin-type recombination is known to be a second order mechanism, leading to nonlinear curves at high light power, whereas trap assisted recombination is a first order mechanism, and thus does not affect the linearity of photocurrent versus light flux curves.[43]

Results plotted in Figure 4b do not show any nonlinearity, suggesting that Langevin recombination is not the dominant mechanism in these samples, at least for the range of light flux investigated in this experiment. This point will be further investigated by simulation in the final section. Moreover, both the dependence of the photocurrent with annealing duration, and the poor value of quantum efficiency reported without initial annealing suggest that recombination mechanisms are indeed present, mostly trap assisted recombination. This point will be further confirmed by others experiments in the following section.

Normalized photocurrents versus applied voltage are plotted in Figure 4c, for each annealing step. The photocurrent normalization consists in dividing by the illuminated current density value at –5 V, according to

$$I_{\text{norm}} = -\frac{I_{\text{light}}(V_a) - I_{\text{dark}}(V_a)}{I_{\text{light}}(-5\text{ V}) - I_{\text{dark}}(-5\text{ V})} \quad (2)$$

This procedure is performed in an attempt to simplify the visual comparison of each curve. As in the EQE experiments, the voltage dependence of the current density improves (i.e., reduced) with annealing time before reaching an optimal annealing point (580 min annealing). Note that the built-in voltage seems almost unchanged during the successive steps, suggesting that contact work functions are not affected by annealing.

Finally, the dark current is recorded for each annealing step (Figure 4d). The dark current density decreases continuously with annealing, scaling by more than 2 decades. Such a trend has been reported in only few other works, presumably because the dark current is typically not a figure of merit of solar cell devices.[66] Moreover, optimized organic solar cell have typically very thin active layers (≈100 nm), and consequently may suffer from additional leakage current induced by pinholes. In some publications, the dependence of the dark current on annealing has been attributed to the reduction of the shunt resistance, possibly burned out by annealing[29] or to a better contact selectivity, induced by changes in the vertical phase composition profile.[67]

To summarize, current–voltage characteristics under dark and illumination show two main trends: the improvement of the photocurrent dependence on the electric field, and the drop in the reverse dark current.

3.4. Infrared EQE Measurements

Following the work of Street et al., IR spectral response experiments were also performed in order to probe the density of states in the energy gap.[40,42] Regions of the absorption curves corresponding to bulk absorption (transition from the HOMO to the LUMO levels of the same semiconductor), charge transfer band-to-band across the donor/acceptor interface, exponential absorption tail, and deep state charge transfer are indicated in **Figure 5**, and the transition mechanisms are presented in **Figure 6**. The optical band gap of P3HT is 1.8 eV whereas the optical band gap of the $PC_{60}BM$ is 2.4 eV.

The most interesting part of the spectral response, below 1.6 eV which is in the regime of charge transfer through gap states, exhibits a marked exponential dependence on photon energy, consistent with an exponential density of states in the band tails. Furthermore, this part of the spectral response is in large part reduced by annealing. The contribution from these gap state-mediated transitions diminishes with increased annealing time. To quantify this effect, a band tail characteristic energy parameter E_0 is extracted using an exponential fit (discussed below, see Equation (6) of the 1.1–1.5 eV energy range, for every spectral response versus photon energy curve. As shown in **Figure 7**, this characteristic energy E_0 decreases with annealing time, which indicates a drastic reduction of the density of trap states within the band gap of the blend layer.

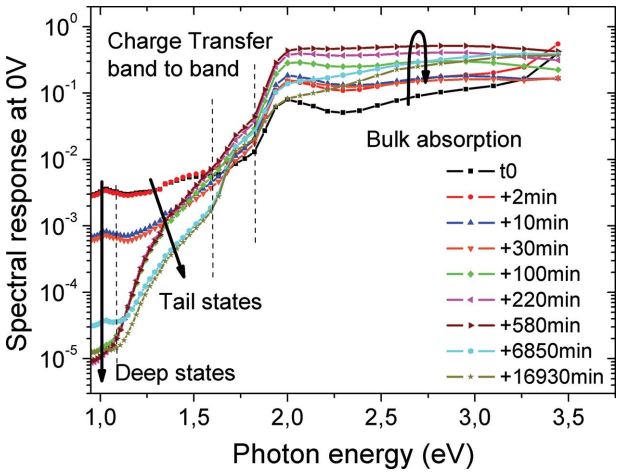

Figure 5. Spectral response measured at short circuit condition as function of the photon energy. Spectral wavelength ranges from 380 nm up to 1400 nm. Different regimes are identified in the figure: bulk absorption for photon energy higher than 1.9 eV, band to band charge transfer for photon energy between 1.9 and 1.6 eV and transition between energy levels located inside the gap and HOMO or LUMO bands below 1.6 eV (see Figure 6 for details).

3.5. Validation of the Band Tail Characteristics Energy Extraction

As mentioned above, the characteristic energy extracted from EQE has been plotted in Figure 7. EQE is only an indirect bulk measurement, which does not directly monitor the density of states into the gap. Indeed, according to a previous study,[68] the absorption coefficient (which is one of the EQE component) for photon energy below the gap is related to the HOMO and LUMO band tails density of states according the following formula (Equation (4))

$$\alpha(h\nu) = C\frac{V_F}{h\nu}\int_{E_{\text{HOMO}}}^{E_{\text{LUMO}}} N_{\text{HOMO}}(E)N_{\text{LUMO}}(E+h\nu)\mathrm{d}E \quad (3)$$

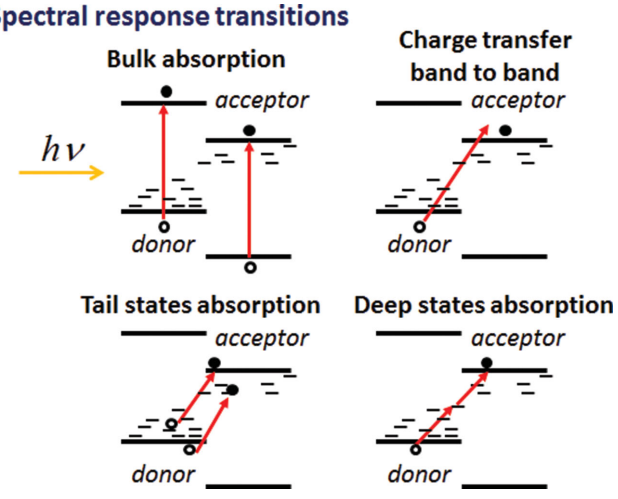

Figure 6. Schematic drawing of the different transitions occurring in a BHJ solar cell.

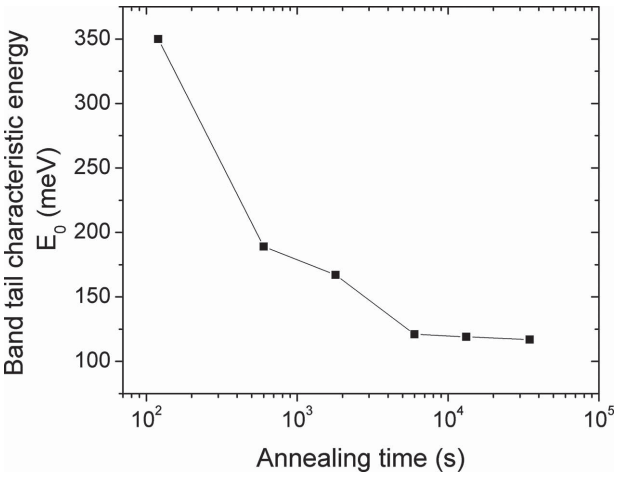

Figure 7. Band tail characteristic energy E_0 extracted from spectral response experiments in the IR regime versus annealing duration using an exponential fitting law.

where V_F is the heterojunction interface volume fraction and C a constant. The absorption coefficient can be divided into a sum of three different contributions: band-to-band transition; band-to-tail or tail-to-band transitions and tail-to-tail transition. Taking into account the characteristic energy E_0 of the respective HOMO and LUMO band tails, the density of states into the gap are given by Equations (4) and (5):

$$N_{\mathrm{HOMO,tail}}(E) = N_{\mathrm{H\_tail}} \exp\left(-\frac{E - E_{\mathrm{HOMO}}}{E_{0\_\mathrm{H}}}\right), E_{\mathrm{HOMO}} < E < E_{\mathrm{LUMO}} \quad (4)$$

$$N_{\mathrm{LUMO,tail}}(E) = N_{\mathrm{L\_tail}} \exp\left(\frac{E - E_{\mathrm{LUMO}}}{E_{0\_\mathrm{L}}}\right), E_{\mathrm{HOMO}} < E < E_{\mathrm{LUMO}} \quad (5)$$

where $N_{\mathrm{H\_tail}}$ and $N_{\mathrm{L\_tail}}$ are the density of states at the tail band edge, $E_{0\_\mathrm{H/L}}$ is band tail characteristics energy of the HOMO and LUMO band tail population, and E_{HOMO} is the HOMO energy, E_{LUMO} is the LUMO energy.

Computing Equation (4), for photon energy between E_g and $E_g/2$ (1.6 and 0.8 eV) the band-to-tail absorption is found to be dominant over the tail-to-tail transition. In this case, the absorption coefficient indeed exhibits an $\exp(h\nu/E_0)$ dependence, where E_0 is the highest band tail characteristics energy between the HOMO and LUMO band. For photon energy below $E_g/2$, Equation (4) shows that absorption only depends on tail-to-tail transition. In this regime, again, an $\exp(h\nu/E_0)$ dependence is found, with however a different E_0 parameter (except if identical band tail characteristics energy is assumed for both the HOMO and LUMO). However, note that this regime of photon energy was not accessible in our experiments.

In conclusion, it is not possible to extract separately from spectral response measurement both the value of the HOMO and LUMO band tail characteristic energy E_{0_HOMO} and E_{0_LUMO}. Only the highest band tail characteristic energy is obtained where band-to-tail or tail-to-band transitions are dominant over the other contributions.

4. Discussion

Here we summarize the experimental results reported in the previous section. The dependence of *I–V* characteristics on annealing time both in illuminated and dark conditions was measured. Results obtained show the existence of a preferred morphology in terms of short-circuit current, together with constant improvement of the fill factor and decrease of the dark current with annealing. Moreover, the blend morphology was characterized by combining AFM and XRD experiments, leading to an accurate description of the P3HT domain evolution versus annealing. Electron and hole mobilities were measured by TOF experiments, indicating no significant evolution of the transport properties with annealing duration. The density of gap states in the materials was found to depend significantly on annealing duration, as shown by spectral response measurements.

In this section, experimental *I–V* curves obtained in both illuminated and dark conditions are investigated using drift and diffusion simulations, carefully calibrated using previously presented characterization results. In particular, the aim of this section is to demonstrate that the dependence of the electrical response (both in dark and illuminated conditions) on annealing is consistent with reorganization of the band tail DOS.

4.1. Drift–Diffusion Simulations and Calibration

The transport of electrons and holes into the blend is modeled using the extensively used effective semiconductor approach proposed by Kostler et al.[69] Simulations parameters can be found in previous publications,[70–73] and are reported in **Table 1**. Electron and hole mobilities are modeled by field-dependent analytical expressions, obtained by fitting TOF experiments. Both mobilities are taken independent of the annealing duration, in agreement with experiments.

The polymer semiconductor is assumed to be intrinsic. In agreement with experiments, the exponential band tail density of states is included, following the model proposed by Urbach[74] and used in amorphous silicon photodiodes.[75]

For the sake of simplicity, the characteristics energy and band tails amplitude of both HOMO and LUMO bands are assumed equal in the simulation. No additional deep traps are implemented in the code. Trap assisted recombination and occupation probability of the tail states are described by the Shockley-Read-Hall formalism (see Figure S4, Supporting Information for details).

Moreover, the HOMO-band-tail-states are assumed to be donorlike while the LUMO-band-tail states are proposed to be acceptorlike:[76] the charge induced by the possible ionisation of these states is accounted into the self-consistent solution of the Poisson equation. Note that trap-assisted recombinations are computed in this work without using any analytical approximations, such as the popular Taylor and Simmons approximation.[77]

The blend morphology is taken into account in the simulation by adjusting both the electron and holes generation and recombination terms. Following a previous study,[78] the generation term is modified to account for the poor exciton dissociation occurring in blend with too large P3HT and $PC_{60}BM$ domains. Similarly, as electron and holes are supposed to recombine mostly at the heterojunction interface, the recombination term

Table 1. Simulation parameters used in this work.

Parameter	Units	Value
Temperature T	K	300
N_c, N_v	cm^{-3}	5×10^{18}
Φ_{PEDOT}–E_{Fermi}	eV	–0.5
$\Phi_{Aluminum}$–E_{Fermi}	eV	0.12
White light power	a.u.	0.25 * AM1.5
Electrical gap E_g	eV	1.6
ITO thickness d_{ITO}	nm	120 nm
PEDOT:PSS thickness d_{PEDOT}	nm	40 nm
Blend thickness d_{OSC}	nm	330
Aluminium thickness d_{Al}	nm	100
Electrical permittivity ε		3
Band tail characteristics energy E_{H_tail}, E_{L_tail}	eV	Variable
DOS at the tail band edge N_{H_tail},N_{L_tail}	cm^{-3}	10^{14}
Capture section of the trap state Γ	cm^2	10^{15}
Thermal velocity V_{th}	cm s^{-1}	2.7×10^6
Elementary mass m_0	kg	8.92×10^{-31}
Effective mass m^*	kg	0.06 m_0

is assumed propositional to the interface volume fraction V_F. Both terms depend on the P3HT average domain size $\square W \square$, which is deduced from the AFM experiments.

Langevin recombination is also included in these simulations, using the well-known $\gamma(np - n_i^2)$ formula. Contrary to several previous works,[79,80] the Langevin prefactor γ is given by its theoretical expression $\gamma = e(\mu_n + \mu_p)/\varepsilon$, which constitutes an upper estimation of the Langevin recombination. The resulting electron (hole) continuity equation is given by

$$\vec{\nabla} \cdot \overrightarrow{\Phi_n} = \frac{2L_{ex}}{\langle W \rangle} \tanh\left[\frac{\langle W \rangle}{2L_{ex}}\right] G - V_F R_{SRH} - V_F \gamma (np - n_i^2) \quad (6)$$

where Φ_n is the flux of electrons (holes), L_{ex} is the exciton diffusion length, G is the optical generation rate, and R_{SRH} is the recombination rate defined from the SRH formalism.

4.2. Comparison between Experimental Photocurrent and Simulations

Experimental photocurrents versus applied voltage curves are compared with simulation for various annealing times. As seen in **Figure 8**, using the calibration explained for Figure 4c, all the data are nicely reproduced by the simulation. Note that only one single fitting parameter is used here: the trap concentration at the band edge N_0. This parameter is fixed at the same value for all the curves.

If the band tail characteristics energy E_0 is arbitrary kept constant in the simulation, the photocurrent field-dependence remains almost unchanged, despite the interface volume fraction V_F, underlying the critical impact of the band tail density of states on photocurrent.

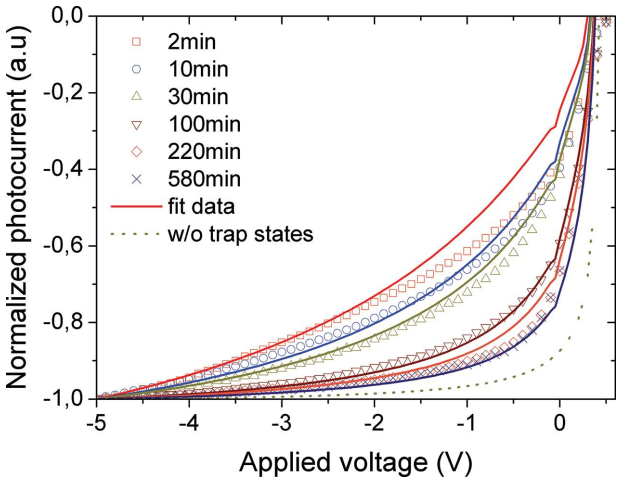

Figure 8. Comparison between experimental and simulated photocurrent I–V curves for the different annealing steps. The evolution of the interface volume fraction V_f (extracted from AFM images) is taken into account in the simulation, as well as the evolution of the band tail characteristic energy E_0 (extracted from EQE experiments).

Similarly, the spectral response under short circuit condition is simulated versus annealing, and plotted together with experimental data in Figure 4a. The simulation parameters are the same as in Figure 8. Simulations qualitatively reproduce the "bell shape" observed in the experiments, and confirm the interpretation of the two part of the curve: exciton dissociation limited at large domain size, and trap assisted recombination at small domain size.

Note that simulations have been performed for a different light power condition than experiments. Indeed, the power used in simulation is 250 W m^{-2}, instead of ≈0.3 W m^{-2} in experiments. This difference however do not impact the comparison, since the short circuit current is indeed linearly dependent on the light power (as confirmed in experiments, see Figure 4b).

4.3. Nongeminate Langevin versus SRH Mechanism

As previously mentioned, recombinations in organic solar cells are usually attributed to either Langevin or Shockley-Read Hall (SRH) mechanisms. The SRH recombination rate is usually proportional to carrier density n, while the Langevin rate is proportional to the square of the carrier density n^2. For this reason, assuming standard value for the Langevin prefactor γ, this later mechanism typically dominates only at high light flux (>1sun) in P3HT/$PC_{60}BM$ blend [80] or in forward bias beyond the built-in potential (OLED device).[81,82] In the literature, this point has been the source of debate.[40,83,84]

In practice, the dominant mechanism can be discriminated by measuring the linearity of the photodiode current as function of light flux. Trap-assisted recombination keeps a linear relation between the short circuit current density and the light intensity, whereas Langevin type recombination induces non-linear effects at high light flux (recombination term proportional to the square of the carrier density).

Numerical simulations were performed to estimate the dominant mechanism in our system (**Figure 9**). It turns out that for the level of traps considered in this work and extracted from

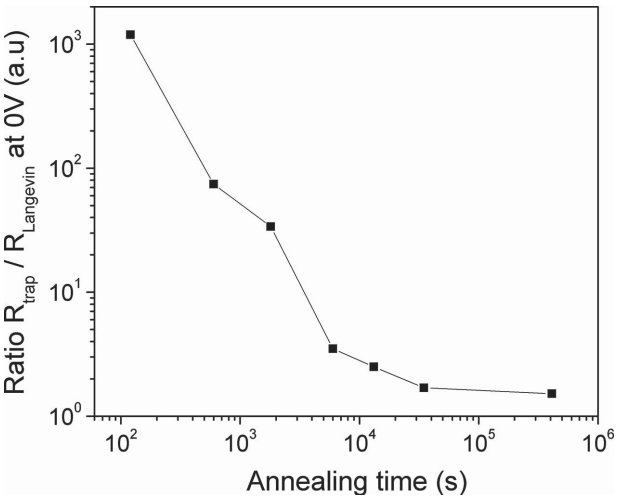

Figure 9. Calculation of the ratio between the SRH recombination and the Langevin recombination terms at short circuit condition as function of the annealing time. For high band tail states, Langevin recombination can be neglected whereas for optimized efficiency, the Langevin term is of the same order of magnitude than the SRH term.

experiments, SRH is always the dominant mechanisms, at least for light power lower than 250 W m^{-2} (the maximum light power value used in this work). However, in the optimum morphology condition, Langevin can be as high as 60% of SRH, suggesting that this former mechanism cannot be ignored. It is likely that, in well optimized blends based on polymers more advanced than P3HT, e.g., low band gap polymers, Langevin might be the most effective recombination mechanism.

4.4. Reverse Dark Currents

Dark currents were also investigated (see **Figure 10** a). In this regime, as there is no light-induced charge generation, only the recombination term is effective. In forward bias, trap states located deeply in the gap help in the recombination of electrons and holes injected into the device (as the carrier concentration in the semiconductor exceeds the intrinsic carrier concentration). In reverse bias however, deep states help in the electron-holes pair generation process. The SRH recombination rate in this latter case is directly proportional to $N_t n_i^2$ (with N_t the trap states concentration), which explains the high dark current level observed at large deep states concentration, i.e., at low annealing time. During the annealing treatment, the reorganization of the band tail DOS induces a lowering of the density of trap states, explaining the drop of the reverse dark current.

In the reverse bias regime, if the model reproduces quite well the amplitude of the dark current versus annealing, the field dependence is not well captured. This difference originates from the transport model in the drift–diffusion approach, which does not account for hopping transport through deep states. This limitation can be partially removed following the approach of Hurkx et al.,[76] which accounts for trap assisted tunneling from the trap state to the HOMO or LUMO bands as illustrated in Figure S4, Supporting Information. When this new approach is implemented, the agreement between experiments and simulations in the negative bias regime appears significantly improved (see Figure 10b). Note that the dark injection from contacts into the trap states is not taken into account in this model. The good agreement between simulations and experiments leads to the conclusion that this effect can be neglected.

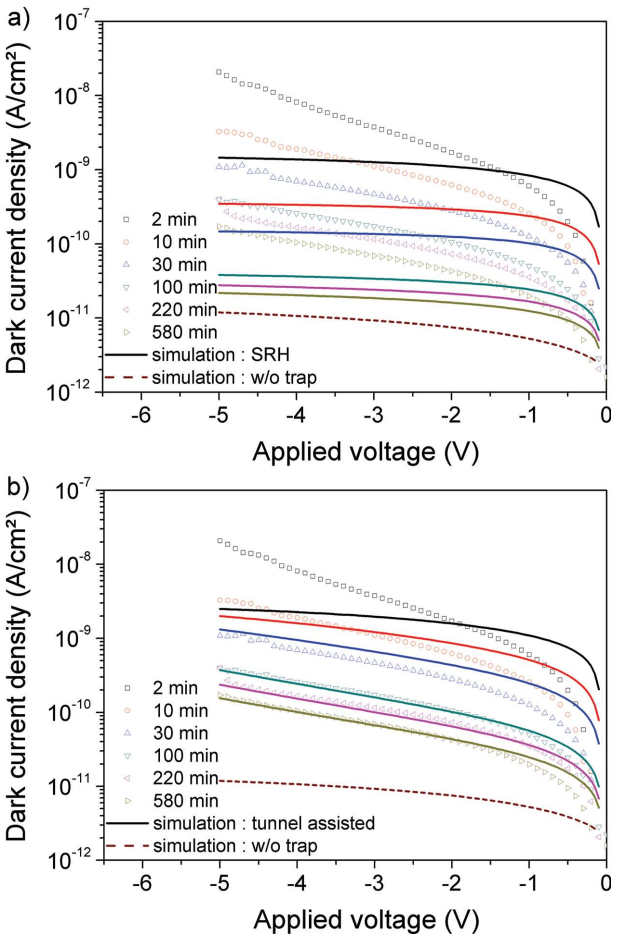

Figure 10. Dark current density versus applied voltage, for several annealing duration using simple trap assisted recombination model (a) or using trap assisted recombination model accounting for tunneling (b). Parameters are the same as Figure 8.

4.5. Charge Transfer State versus SRH Recombination

Charge transfer (CT) state recombination has recently been extensively investigated in the literature[85–87] and should be discussed as a possible alternative explanation of the impact of thermal annealing on the performance of organic solar cells. This third mechanism implies geminate recombination[88] and depends mostly on the organization of the fullerene phase with respect to the polymer domains. Friend and co-workers[87] have recently demonstrated that the presence of pure fullerene domains, at least 5 nm in size, entirely suppresses CT recombination. In this work, the introduction of annealing temperature leads to an improvement of device performance, which could be attributed to a change in the fullerene domain organization and thus to a possible diminution of the CT state recombination.

This effect is certainly present in our results, especially at low electric fields, where charge transfer state recombination is more efficient. Note that it is partially included in our simulation, as the Onsager–Braun model is implemented. However, this approach is not completely satisfactory, as it does not include any morphological dependence of the recombination probability.[86]

Nonetheless, we believe that the morphology dependence of CT recombination cannot explain all of our experimental results, and that our hypothesis (SRH recombination) is also needed, as discussed in this paper. Let us summarize the arguments in favor of SRH versus CT recombination.

First of all, EQE experiments at low photon energy clearly indicate the presence of shallow and deep traps in the energy gap, and allow for quantification of the impact of thermal annealing on their concentration. This effect is unlikely to be explained by pure CT recombination. Moreover, our model, accounting only for electron–hole pairs generation, nongeminate Langevin and SRH recombination, can nicely reproduce *I–V* curves under illumination at all temperature annealing. There are no fitting parameters in these simulations: mobility, domain size, and trap concentrations all have been extracted from complementary experiments (time of flight for mobility, AFM, and X-ray diffraction measurement for the domain size, and EQE at low energy for the trap concentration). Last but not least, the same model also explains, again without additional fitting parameters, the impact of annealing on the dark currents, where CT recombination is expected to be absent (no light). These conclusions, in the case of P3HT:PC_{60}BM blends, are consistent with other works.[88,89]

All these facts support the analysis presented in this work, even if more investigation is needed to quantify more accurately the impact of CT recombination.

The origin of the traps observed here through infrared EQE measurements is not known. Different hypotheses are mentioned in the literature. The band tail states may originate from the polymer chain disorder inside the active layer,[42,90] confirmed by UPS measurements[91] and by quantum chemistry simulations.[92] Defects can also induce traps, but not necessarily "band tails." Localized traps may originate from polymer chain scission[93] or impurities such as oxygen.[94] or metallic residues[95]

5. Conclusions

In this work, trap assisted recombinations have been investigated, focusing in particular on the impact of thermal annealing durations in the classical P3HT:PC_{60}BM solar cells. Interestingly, while the spectral response versus annealing time exhibits a bell curve with an optimum value, the dark currents however are monotonously reduced by annealing. The second part of the spectral response (i.e., decrease of the efficiency) is interpreted in term of blend morphology change. Indeed AFM and X-rays diffraction measurements have revealed that the growth of P3HT domains occurs in the 2D longitudinal directions. When the average polymer domain width exceeds the exciton diffusion length, the solar cell efficiency gets lower because of the exciton dissociation rate limitation.

On the other hand, this work demonstrates that the initial improvement of the spectral response is not correlated to any carrier mobility improvement as confirmed by time-of-flight experiments, where mobilities for both hole and electron have been extracted and found unchanged during the annealing steps.

The impact of thermal annealing durations on the trap assisted recombination rate has been investigated to explain both dark and light current changes. First, the existence of exponential band tails into the gap has been experimentally confirmed by measuring the device spectral response in the IR regime. Such method revealed the existence of large density of states into the gap, largely reduced by the successive annealing steps.

All these results (mobility, band tails) have then been used to calibrate drift and diffusion simulations. It turns out that electrical and optical simulations can satisfactory reproduce illuminated and dark experimental currents at the same time, versus voltage and annealing time. These simulations highlight the predominance of the band tail states reorganization in the improvement of the solar cell characteristics. Recombinations assisted by trap states are lowered by annealing, which lead to an improvement of the solar cell efficiency and a decrease of the reverse dark current (thermal generation from trap states). This approach constitutes a powerful physical model, able to explain the existence of an ideal morphology for photogenerated currents, and at the same time, able to capture the constant reduction of dark current induced by annealing. An optimum in term of quantum efficiency is found between the band tail states reorganization and the coarsening of the blend morphology as function of thermal annealing duration.

6. Experimental Section

Optoelectrical Characterization: Encapsulated devices were characterized in ambient air. Optoelectrical measurements are performed on a dedicated optical bench. The devices are placed in a light shielding box and can be illuminated by a specific optical head controlling the size of the spot light on the device and insuring in-line measurement of the light power. All light sources are placed outside of the shielding box and connected to the optical head by a liquid light-guide. Current–voltage (*I–V*) characteristics were measured with a Keithley 2636A in darkness and under illumination (irradiance of 200 W m^{-2}) obtained from a quartz tungsten halogen lamp (LOT-Oriel 250W QTH light source). For photodiode linearity measurement, the irradiance is reduced by insertion of different optical densities. Photocurrents were recorded as function of incident light power. For spectral response measurement, a 1/4 m grating spectrometer (LOT-Oriel Cornerstone 130) with a resolution of 20 nm was used. The EQE measurements were performed at zero-bias voltage to get the lowest dark current. The incident light power was measured with a calibrated photodiodes: silicon sensor for wavelengths below 900 nm and an InGaAs sensor up to 1.7 µm.

AFM Characterization: AFM phase measurements of the blend surface were performed in air on specific separated samples using a Veeco Multimode AFM in tapping mode. AFM tips (super sharp silicon tip purchased from NanoSensors) with 2 nm radius and resonance 300 kHz frequency were used in order to identify the different phases on fine blend morphology. This insured clear distinction between crystallized and amorphous region on the blend surface. The detector side of the AFM had an aluminum coating in order to improve the signal detection.

Supporting Information

Supporting Information is available from the Wiley Online Library or from the author.

Acknowledgements

The authors are grateful to Simon Charlot for photodiodes preparation and discussions regarding solar cell fabrication. The work done at CEA was supported by ISORG. Work in Princeton was supported in part by the National Science Foundation (Grant No. DMR-1005892).

Received: May 20, 2014
Revised: December 2, 2014
Published online: January 5, 2015

[1] K. M. Coakley, M. D. McGehee, *Chem. Mater.* **2004**, *16*, 4533.
[2] J. Peet, M. L. Senatore, A. J. Heeger, G. C. Bazan, *Adv. Mater.* **2009**, *21*, 1521.
[3] M. A. Brady, G. M. Su, M. L. Chabinyc, *Soft Matter* **2011**, *7*, 11065.
[4] G. Li, R. Zhu, Y. Yang, *Nat. Photonics* **2012**, *6*, 153.
[5] C. W. Tang, *Appl. Phys. Lett.* **1986**, *48*, 183.
[6] *NREL's Best Research Cell Efficiencies* as of November 2013.
[7] G. Yu, J. Gao, J. Hummelen, F. Wudl, A. J. Heeger, *Science* **1995**, *270*, 1789.
[8] N. S. Sariciftci, L. Smilowitz, A. J. Heeger, F. Wudl, *Science* **1992**, *258*, 1474.
[9] J. J. M. Halls, K. Pichler, R. H. Friend, S. C. Moratti, A. B. Holmes, *Appl. Phys. Lett.* **1996**, *68*, 3120.
[10] J. K. J. van Duren, X. Yang, J. Loos, C. W. T. Bulle-Lieuwma, A. B. Sieval, J. C. Hummelen, R. A. J. Janssen, *Adv. Funct. Mater.* **2004**, *14*, 425.
[11] P. K. Watkins, A. B. Walker, G. L. B. Verschoor, *Nano Lett.* **2005**, *5*, 1814.
[12] X. Yang, J. Loos, S. C. Veenstra, W. J. H. Verhees, M. M. Wienk, J. M. Kroon, M. A. J. Michels, R. A. J. Janssen, *Nano Lett.* **2005**, *5*, 579.
[13] M. Campoy-Quiles, T. Ferenczi, T. Agostinelli, P. G. Etchegoin, Y. Kim, T. D. Anthopoulos, P. N. Stavrinou, D. D. C. Bradley, J. Nelson, *Nat. Mater.* **2008**, *7*, 158.
[14] H. Hoppe, N. Arnold, D. Meissner, N. S. Sariciftci, *Thin Solid Films* **2004**, *451*, 589.
[15] M. C. Heiber, A. Dhinojwala, *J. Chem. Phys.* **2012**, *137*, 014903.
[16] R. R. Lunt, J. B. Benziger, S. R. Forrest, *Adv. Mater.* **2010**, *22*, 1233.
[17] F. Yang, S. R. Forrest, *ACS Nano* **2008**, *2*, 1022.
[18] M. Dante, J. Peet, T.-Q. Nguyen, *J. Phys. Chem. C* **2008**, *112*, 7241.
[19] L. F. Drummy, R. J. Davis, D. L. Moore, M. Durstock, R. A. Vaia, J. W. P. Hsu, *Chem. Mater.* **2011**, *23*, 907.
[20] W. Ma, C. Yang, A. J. Heeger, *Adv. Mater.* **2007**, *19*, 1387.
[21] V. D. Mihailetchi, H. X. Xie, B. de Boer, L. J. A. Koster, P. W. M. Blom, *Adv. Funct. Mater.* **2006**, *16*, 699.
[22] Y. Kim, S. A. Choulis, J. Nelson, D. D. C. Bradley, S. Cook, J. R. Durrant, *Appl. Phys. Lett.* **2005**, *86*, 063502.
[23] J. Peet, J. Y. Kim, N. E. Coates, W. L. Ma, D. Moses, A. J. Heeger, G. C. Bazan, *Nat. Mater.* **2007**, *6*, 497.
[24] J. K. Lee, W. L. Ma, C. J. Brabec, J. Yuen, J. S. Moon, J. Y. Kim, K. Lee, G. C. Bazan, A. J. Heeger, *J. Am. Chem. Soc.* **2008**, *130*, 3619.
[25] F. C. Krebs, *Sol. Energy Mater. Sol. Cells* **2009**, *93*, 394.
[26] C. N. Hoth, S. A. Choulis, P. Schilinsky, C. J. Brabec, *Adv. Mater.* **2007**, *19*, 3973.
[27] H. Hoppe, N. S. Sariciftci, *J. Mater. Chem.* **2006**, *16*, 45.
[28] C. Müller, T. A. M. Ferenczi, M. Campoy-Quiles, J. M. Frost, D. D. C. Bradley, P. Smith, N. Stingelin-Stutzmann, J. Nelson, *Adv. Mater.* **2008**, *20*, 3510.
[29] F. Padinger, R. S. Rittberger, N. S. Sariciftci, *Adv. Funct. Mater.* **2003**, *13*, 85.
[30] T. Erb, U. Zhokhavets, G. Gobsch, S. Raleva, B. Stühn, P. Schilinsky, C. Waldauf, C. J. Brabec, *Adv. Funct. Mater.* **2005**, *15*, 1193.
[31] L. H. Nguyen, H. Hoppe, T. Erb, S. Günes, G. Gobsch, N. S. Sariciftci, *Adv. Funct. Mater.* **2007**, *17*, 1071.
[32] U. Zhokhavets, T. Erb, H. Hoppe, G. Gobsch, N. S. Sariciftci, *Thin Solid Films* **2006**, *496*, 679.
[33] D. Chirvase, J. Parisi, J. C. Hummelen, V. Dyakonov, *Nanotechnology* **2004**, *15*, 1317.
[34] W. Ma, C. Yang, X. Gong, K. Lee, A. J. Heeger, *Adv. Funct. Mater.* **2005**, *15*, 1617.
[35] L. Zeng, C. W. Tang, S. H. Chen, *Appl. Phys. Lett.* **2010**, *97*, 053305.
[36] R. A. Marsh, C. Groves, N. C. Greenham, *J. Appl. Phys.* **2007**, *101*, 083509.
[37] L. Meng, D. Wang, Q. Li, Y. Yi, J.-L. Brédas, Z. Shuai, *J. Chem. Phys.* **2011**, *134*, 124102.
[38] B. Ray, M. A. Alam, *Sol. Energy Mater. Sol. Cells* **2012**, *99*, 204.
[39] L. J. A. Koster, O. Stenzel, S. D. Oosterhout, M. M. Wienk, V. Schmidt, R. A. J. Janssen, **2013**, *3*, 615.
[40] R. A. Street, M. Schoendorf, *Phys. Rev. B* **2010**, *81*, 1.
[41] R. A. Street, S. R. Cowan, A. J. Heeger, *Phys. Rev. B* **2010**, *82*, 11.
[42] R. A. Street, A. Krakaris, S. R. Cowan, *Adv. Funct. Mater.* **2012**, *22*, 4608.
[43] L. Dou, J. You, Z. Hong, Z. Xu, G. Li, R. A. Street, Y. Yang, *Adv. Mater.* **2013**, *25*, 6642.
[44] S. J. Lou, J. M. Szarko, T. Xu, L. Yu, T. J. Marks, L. X. Chen, *J. Am. Chem. Soc.* **2011**, *133*, 20661.
[45] S. Imamura, K. Palanisamy, S. Kannappan, S. Ochiai, *J. Korean Phys. Soc.* **2012**, *61*, 464.
[46] E. J. Spadafora, R. Demadrille, B. Ratier, B. Grévin, *Nano Lett.* **2010**, *10*, 3337.
[47] B. Ray, M. A. Alam, *Appl. Phys. Lett.* **2011**, *99*, 033303.
[48] H. Sirringhaus, P. Brown, R. Friend, *Nature* **1999**, *401*, 685.
[49] W. Yin, M. Dadmun, *ACS Nano* **2011**, *5*, 4756.
[50] D. Chen, A. Nakahara, D. Wei, D. Nordlund, T. P. Russell, *Nano Lett.* **2011**, *11*, 561.
[51] B. A. Collins, E. Gann, L. Guignard, X. He, C. R. McNeill, H. Ade, *J. Phys. Chem. Lett.* **2010**, *1*, 3160.
[52] N. D. Treat, M. A. Brady, G. Smith, M. F. Toney, E. J. Kramer, C. J. Hawker, M. L. Chabinyc, *Adv. Energy Mater.* **2011**, *1*, 82.
[53] D. R. Kozub, K. Vakhshouri, L. M. Orme, C. Wang, A. Hexemer, E. D. Gomez, *Macromolecules* **2011**, *44*, 5722.
[54] M. Pfannmöller, H. Flügge, G. Benner, I. Wacker, C. Sommer, M. Hanselmann, S. Schmale, H. Schmidt, F. A. Hamprecht, T. Rabe, W. Kowalsky, R. R. Schröder, *Nano Lett.* **2011**, *11*, 3099.
[55] U. Vongsaysy, B. Pavageau, G. Wantz, D. M. Bassani, L. Servant, H. Aziz, *Adv. Energy Mater.* **2014**, *4*, 3.
[56] H. Scher, E. Montroll, *Phys. Rev. B* **1975**, *12*, 2455.
[57] S. Tiwari, N. C. Greenham, *Opt. Quantum Electron.* **2009**, *41*, 69.
[58] F. Monestier, J.-J. Simon, P. Torchio, L. Escoubas, F. Flory, S. Bailly, R. de Bettignies, S. Guillerez, C. Defranoux, *Sol. Energy Mater. Sol. Cells* **2007**, *91*, 405.
[59] M. M. Mandoc, W. Veurman, J. Sweelssen, M. M. Koetse, P. W. M. Blom, *Appl. Phys. Lett.* **2007**, *91*, 073518.
[60] V. D. Mihailetchi, H. Xie, B. de Boer, L. M. Popescu, J. C. Hummelen, P. W. M. Blom, L. J. A. Koster, *Appl. Phys. Lett.* **2006**, *89*, 012107.
[61] E. Couderc, N. Bruyant, A. Fiore, F. Chandezon, D. Djurado, P. Reiss, J. Faure-Vincent, *Appl. Phys. Lett.* **2012**, *101*, 133301.

[62] V. Kažukauskas, M. Pranaitis, V. yras, L. Sicot, F. Kajzar, *Thin Solid Films* **2008**, *516*, 8988.
[63] H. Bassler, *Phys. Status Solidi* **1993**, *175*, 15.
[64] L. Zeng, W. T. Ching, H. C. Shaw, *Appl. Phys. Lett.* **2010**, *97*, 5.
[65] B. C. Thompson, J. M. J. Fréchet, *Angew. Chem., Int. Ed.* **2008**, *47*, 58.
[66] K.-J. Baeg, M. Binda, D. Natali, M. Caironi, Y.-Y. Noh, *Adv. Mater.* **2013**, *25*, 4267.
[67] T. Agostinelli, M. Campoy-Quiles, J. C. Blakesley, R. Speller, D. D. C. Bradley, J. Nelson, *Appl. Phys. Lett.* **2008**, *93*, 203305.
[68] R. A. Street, K. Song, J. Northrup, S. R. Cowan, *Phys. Rev. B* **2011**, *83*, 1.
[69] L. J. A. Koster, E. Smits, V. D. Mihailetchi, P. W. M. Blom, *Phys. Rev. B* **2005**, *72*, 1.
[70] J. Cuiffi, T. Benanti, W. J. Nam, S. Fonash, *Appl. Phys. Lett.* **2010**, *96*, 143307.
[71] S. Altazin, R. Clerc, R. Gwoziecki, G. Pananakakis, G. Ghibaudo, C. Serbutoviez, *Appl. Phys. Lett.* **2011**, *99*, 143301.
[72] J. Cao, Z. Zhan, L. Hou, Y. Long, P. Liu, W. Mai, *Appl. Opt.* **2012**, *51*, 5718.
[73] R. Häusermann, E. Knapp, M. Moos, N. A. Reinke, T. Flatz, B. Ruhstaller, *J. Appl. Phys.* **2009**, *106*, 104507.
[74] F. Urbach, *Phys. Rev.* **1953**, *92*, 1324.
[75] I. Sakata, Y. Hayashi, *Appl. Phys. A* **1985**, *164*, 153.
[76] G. A. M. Hurkx, D. B. M. Klaassen, M. P. G. Knuvers, *IEEE Trans. Electron. Dev.* **1992**, *39*, 331.
[77] J. Simmons, G. Taylor, *Phys. Rev. B* **1971**, *4*, 502.
[78] B. Ray, M. A. Alam, *Appl. Phys. Lett.* **2011**, *99*, 033303.
[79] G.-J. A. H. Wetzelaer, N. J. Van der Kaap, L. J. A. Koster, P. W. M. Blom, *Adv. Energy Mater.* **2013**, *3*, 1130.
[80] M. Lenes, L. J. A. Koster, V. D. Mihailetchi, P. W. M. Blom, *Appl. Phys. Lett.* **2006**, *88*, 052104.
[81] G. A. H. Wetzelaer, M. Kuik, H. Nicolai, P. W. M. Blom, *Phys. Rev. B* **2011**, *83*, 165204.
[82] M. Kuik, L. J. A. Koster, A. G. Dijkstra, G. A. H. Wetzelaer, P. W. M. Blom, *Org. Electron.* **2012**, *13*, 969.
[83] C. Deibel, A. Wagenpfahl, *Phys. Rev. B* **2010**, *82*, 207301.
[84] R. A. Street, *Phys. Rev. B* **2010**, *82*, 207302.
[85] M. Hallermann, I. Kriegel, E. Da Como, J. M. Berger, E. Von Hauff, J. Feldmann*Adv. Funct. Mater.* **2009**, *19*, 22.
[86] B. M. Savoie, A. Rao, A. A. Bakulin, S. Gelinas, B. Movaghar, R. H. Friend, T. J. Marks, M. A. Ratner, *J. Am. Chem. Soc.* **2014**, *136*, 7.
[87] S. Gélinas, A. Rao, A. Kumar, S. L. Smith, A. W. Chin, J. Clark, T. S. Van Der Poll, G. C. Bazan, R. H. Friend, *Science* **2014**, *343*, 6170.
[88] A. J. Heeger, *Adv. Mater.* **2014**, *26*, 1.
[89] R. A. Street, S. R. Cowan, A. J. Heeger, *Phys. Rev. B* **2011**, *83*, 035205.
[90] Z. M. Beiley, E. T. Hoke, R. Noriega, J. Dacuña, G. F. Burkhard, J. A. Bartelt, A. Salleo, M. F. Toney, M. D. McGehee, *Adv. Energy Mater.* **2011**, *1*, 5.
[91] F. Bussolotti, S. Kera, K. Kudo, A. Kahn, N. Ueno, *Phys. Rev. Lett.* **2013***110*, 26.
[92] J. Rivnay, R. Noriega, J. E. Northrup, R. J. Kline, M. F. Toney, A. Salleo, *Phys. Rev. B* **2011**, *83*, 12.
[93] R. A. Street, J. E. Northrup, B. S. Krusor, *Phys. Rev. B* **2012**, *85*, 20.
[94] A. Seemann, H. J. Egelhaaf, C. J. Brabec, J. A. Hauch, *Org. Electron.* **2009**, *10*, 8.
[95] M. P. Nikiforov, B. Lai, W. Chen, S. Chen, R. D. Schaller, J. Strzalka, J. Maser, S. B. Darling, *Energy Environ. Sci.* **2013**, *6*, 5.